On the influence of AgMg precursor formation on MgAgSb microstructure and thermoelectric properties

Ignacio Rodriguez-Barber[1,2], Julia Camut[1], Laura Luhmann[1,2], Aidan Cowley[2], Eckhard Mueller[1,3] and Johannes de Boor[1]

[1] Institute of Materials Research, German Aerospace Center, Linder Hoehe, 51147 Cologne, Germany; julia.camut@dlr.de; laura.luhmann@dlr.de; eckhard.mueller@dlr.de; johannes.deboor@dlr.de

[2] European Astronaut Center, European Space Agency, Linder Hoehe, 51147 Cologne, Germany; aidan.cowley@esa.int

[3] Institute of Inorganic and Analytical Chemistry, Justus Liebig University Giessen, Heinrich-Buff-Ring 17, 35392 Giessen, Germany

Corresponding authors: Ignacio Rodriguez-Barber i.rodriguezbarber@gmail.com; Johannes de Boor johannes.deboor@dlr.de

Abstract

α-MgAgSb has been identified as promising thermoelectric material, with peak performance around 300ºC, filling the gap between low- and high-temperature thermoelectric materials. The complexity of the Mg-Ag-Sb phase diagram and the sensitivity of the MgAgSb synthesis process often leads to impurities appearing in the final samples, which reduce the thermoelectric figure of merit zT. Using a two-step ball milling process, we show that the extent of the AgMg precursor formation has a direct effect on the final composition, mainly with respect to the dyscrasite (Ag_3Sb) content. We study how extending the first ball milling step, adding a AgMg sintering step before the second ball milling step or reducing the Ag particle size each affect the overall formation of AgMg. It is shown that lower Ag wt. % in said precursor results in lower Ag_3Sb content in the final samples, achieving <1 wt% Ag_3Sb when Ag <1wt.% (in the precursor). This leads to a 23 % improvement of zT between 300 and 563 K and a peak value of ~1.2 at 500 K. This shows that the complete conversion of Mg and Ag into AgMg is the key for high performance α-MgAgSb.

Keywords: thermoelectric materials, semiconductors, mechanical alloying, sintering, impurities in semiconductors

1. Introduction

Over the past years, more efficient and sustainable ways of supplying energy have been and are still being investigated. Thermoelectric materials are amongst the considered solutions. Their ability to convert heat directly into electricity and vice versa makes them suitable candidates for refrigeration and heat recovery applications. In areas like the automotive, steelmaking or cement industries, thermoelectric generators (TEGs) can be used to partially recover the energy lost in the form of heat waste [1,2]. TEGs are also used in the space industry, powering deep-space probes, such as the Voyager 1 and 2, and are one of the suggested options for lunar energy production through heat harvesting [3–6].

The potential of a thermoelectric material for waste heat recovery applications is determined by its unitless figure of merit $zT = \frac{\sigma \cdot S^2 \cdot T}{\kappa}$, where σ is the electrical conductivity, S the Seebeck coefficient and κ the thermal conductivity, with a benchmark value of ~1 (thermoelectric materials with zT close to or over unity are considered to have good performance). In order to maximize their efficiency, both a high power factor $PF = \sigma \cdot S^2$ and a low thermal conductivity κ are needed. Amongst the optimized, commercially available thermoelectric materials Te-based

($Bi_xSb_{2-x}Te_3$) solid solutions for near room temperature applications can be found. Extensive research has been conducted on high-temperature thermoelectrics, such as Half-Heusler compounds, Skutterudites or $Mg_2(Si,Sn)$ solid solutions [7–11].

In the last decade, MgAgSb-based materials have been investigated as promising p-type, low- and medium-temperature thermoelectrics, which could fill the gap between Bi_2Ti_3 and the high-temperature materials. In addition to their good thermoelectric performance in the mentioned temperature gap, they also present higher mechanical properties, namely hardness, fracture toughness and compressive strength than other p-type thermoelectric materials, thus making it more advantageous for realistic applications[12,13]. Kirkham et al. first described, in 2012, the three temperature-dependent crystal structures of this material system (α-, β-, and γ-MgAgSb). Only its low-temperature phase (α-MgAgSb), stable up to 573 K, was found to have good thermoelectric properties, with a maximum *zT* around 0.5 despite a high concentration of Ag_3Sb and Sb impurities [14]. Several studies have been conducted with the objective of optimizing the composition and improving the overall performance of MgAgSb, using different strategies to produce pure, good-performing samples. These include planetary ball milling (PBM) followed by sintering and annealing [13,14], melting combined with an annealing process [15,16], and microwave-assisted melting [19]. The best results for undoped MgAgSb obtained thus far were achieved through the two-step high-energy ball milling (first step: ball milling of Ag and Mg, second step: addition of Sb) and sintering method first presented by Zhao et al., with Ag- and Sb-deficient stoichiometries [20]. Using this method, and by slightly tuning the composition, an average zT of 1.1 between room temperature and 548 K is achieved for $MgAg_{0.97}Sb_{0.995}$ [21], the highest reported value for undoped MgAgSb. Several doping agents have been tested in order to enhance the thermoelectric properties [14,16,18,20–23], obtaining peak values of zT ~1.4 at 475 K for Ni-doping in the Ag sites [20]. However, and despite the good performance of MgAgSb-based samples obtained through the two-step ball milling process, its synthesis remains a major challenge, as it is required to tune the (nominal) composition very finely and it is not uncommon to find impurities [24–26], for the window of stability of MgAgSb is small [29]. The most common secondary phases are dyscrasite (Ag_3Sb) and antimony [13–16,26]. These impurities have clear detrimental effects on the final thermoelectric properties and are a major impediment to achieve the best possible values for *zT* [30], but their mechanism of formation has not been studied in detail, nor how they can be avoided. Given the complexity of the Mg-Ag-Sb phase diagram and the complexity of the MgAgSb synthesis process, a good understanding of the mechanisms of formation of the different phases is required.

One of the suspected reasons behind the recurrent appearance of impurities is the insufficient formation of AgMg (as a precursor to form MgAgSb), thus the interest in a two-step ball milling process. In the synthesis of MgAgSb through mechanical means, Ag seams to react with Sb preferentially, forming Ag_3Sb (or compounds with similar compositions). Therefore, in order to avoid the appearance of such secondary phase, it is necessary to minimize the amount of elemental Ag before Sb is added to the mix. In this report, we study how the formation of the AgMg precursor affects the final composition and microstructure of α-MgAgSb. We use three different approaches to produce AgMg powder: (i) extending the first ball milling step (with Ag and Mg only) to increase the degree of precursor formation due to mechanical alloying, (ii) combining ball milling with a short sintering step and (iii) reducing the initial particle size before milling. The results show a clear correlation between weight % of elemental Ag in the precursor and the final content of Ag_3Sb in MgAgSb samples. We also present the final thermoelectric properties of MgAgSb samples obtained following all three different routes and show improved performance with decreased secondary phase content.

2. Materials and Methods

A two-step ball milling process followed by direct sintering, similar to that reported by Liu et al. [21] was used to produce α-MgAgSb samples. Pure elements were weighed according to nominal composition $MgAg_{0.97}$ (Mg: turnings, Merck KGaA, >99%; Ag: granules, 1-6 mm, Sindlhauser Materials GmbH, 99.99%) and loaded in a stainless steel jar (65 mL) with two stainless steel balls (12.7 mm) under Ar atmosphere. After high-enery ball milling (HEBM) for 8 h (SPEX SamplePrep 8000D Mixer/Mill), Sb was weighed and added to the mix to obtain $MgAg_{0.97}Sb_{0.995}$ (Sb: granules, 1-3 mm, Evochem GmbH, 99.99%), then milled for 5 more hours. The powder obtained thereby was stored in an Ar glovebox prior to the sintering step or any characterization process. It was pressed for 8 min at 573 K under 85 MPa and direct current, using 12.7 mm graphite dies (Dr Fritsch DSP510). Note that the sintering temperature is considerably lower than that used for other Mg-based thermoelectric materials like Mg_2Si or Mg_3Sb_2, usually processed between 900 and 1100 K [31–36], and Mg loss is therefore not expected to occur. Due to the observed insufficient reaction between Ag and Mg in the first ball milling step we have also modified the synthesis process for AgMg, either by extending the ball milling, by combining ball milling and sintering or by reducing the initial Ag particle size (Ag powder, <45 μm, GoodFellow, 99.99%). The milling times and pressing conditions differing from the reference are specified in the respective results sections.

The Electrical conductivity σ and the Seebeck coefficient S were measured with an in-house device [37]. The Thermal diffusivity α was measured using an LFA 427 or an XFA 467 HT Hyperflash (NETZSCH), and from this, the thermal conductivity κ was calculated as $\kappa = \alpha \cdot C_p \cdot \rho$, where C_p is the heat capacity at constant pressure and ρ is sample density. Constant C_p values can be assumed for this system and temperature range (obtained using the Dulong-Petit law)[20] and ρ was calculated through the Archimedes method. κ_{lat} (the lattice contribution to the thermal conductivity) is approximated as κ-κ_e. The measurement uncertainties for S, σ, and κ are ± 5 %, ± 5 % and ± 8 % respectively. XRD data was obtained using a Bruker D5000 with a secondary monochromator, Cu-Kα radiation (1.5406 Å), step size 0.01º in the 2θ range 20-80º, both for powder and bulk samples. Phase compositions were obtained from XRD spectra through Rietveld refinement, using TOPAS. SEM and EDX characterization were performed using a Zeiss Ultra 55 SEM device.

3. Results

3.1. Extended ball milling step

A first strategy followed to enhance AgMg formation was extending the first ball milling step of the process (originally 8 h in [21]). HEBM does not only reduce particle size, but it also induces mechanical alloying, i.e. a solid state chemical reaction between the precursors. Powder samples were retrieved after 10, 15, 20 and 30 hours of HEBM. XRD scans of these samples reveal a progressive formation of AgMg through ball milling, with higher content of the compound for longer milling times (Figure 1). After 10 hours of ball milling, we find approximately 48 wt. % AgMg in the powder, and we can also observe very clear Ag and Mg peaks. The phase composition evolves through further ball milling, up to 30 hours, where no Ag or Mg peaks can be observed anymore. However, careful examination of a sintered AgMg pellet (using 30 h ball milled powder) does reveal a small Ag peak. Detailed phase composition of all samples can be found in Table 1. For powder samples milled for 15 hours or longer, no Mg peaks are observed in the range of detection of our XRD set-up, only Ag and AgMg. We cannot completely dismiss the existence of pure Mg in the powder due to the sensitivity of XRD. However, the coexistence of AgMg and Ag in a mix with no elemental Mg could be explained due to the fact that AgMg has a window of composition going from 30 to 65 Ag atomic %, depending on temperature[38]. This phenomenon, combined with the overlap between the main Ag and AgMg peaks, can also

explain the observed slight shift of the AgMg peaks towards higher angles with increasing milling duration.
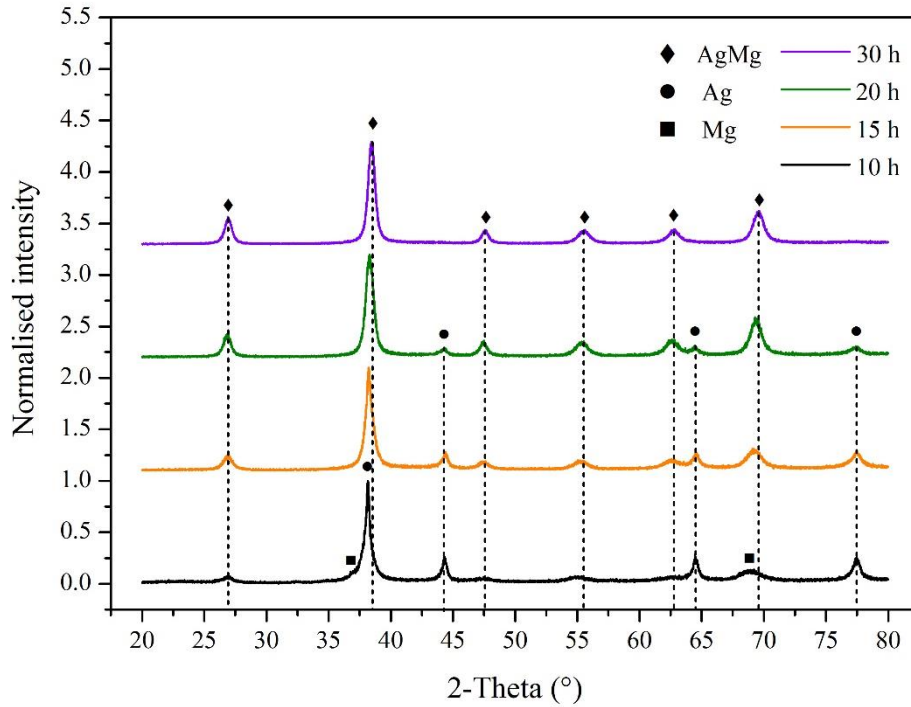

Figure 1: XRD scans of powder samples containing Ag and Mg after 10, 15, 20 and 30 hours of ball milling. Dashed lines indicate position of main AgMg peaks, while markers for Ag and Mg indicate the position of elemental peaks.

Ball milling time	AgMg wt. %	Ag wt. %	Mg wt. %
10 h	47.7	40.3	12
15 h	75.7	24.3	0
20 h	93.1	6.9	0
30 h	97.5	2.5	0

Table 1: phase composition of powder samples containing Ag and Mg after 10, 15, 20 and 30 hours of ball milling

Extending the milling time induces further mechanical alloying between Ag and Mg, increasing the MgAg fraction from 47.7 wt. % after 10 hours to 97.5 % after 30 hours.

3.2. Combination of ball milling and sintering for AgMg formation

A second strategy for AgMg formation consists in combining a first ball milling step with sintering and then crushing of the sintered pellets to obtain AgMg powder. The sintering step is expected to induce faster reaction between both elements, which would result in a reduction of the necessary time to produce the precursor (this is, compared to 30 h).

First, the Mg turnings and Ag granules are milled in the HEBM for 12 hours to ensure homogeneity of the powder. This powder is then sintered for 8 minutes, under 85 MPa, at 3 different temperatures: 573, 623 and 673 K. Higher temperatures were avoided to prevent Mg loss. The XRD scans for the milled powder, as well as for the pressed pellets, can be found in Figure 2. After 12 hours of ball milling there are clear Ag peaks in agreement with the previous study on ball milling duration3.1. The following sintering step seemingly induces further reaction between pure Ag and the AgMg phase (the reaction is mostly between Ag and Ag-deficient AgMg phase). Again, the existence of pure Mg before sintering cannot be discarded due to the limitations of XRD scanning and its resolution. The higher the sintering temperature,

the lower the final elemental Ag content, as can be seen in Table 2. However, even at 673 K there is a non-negligible amount of elemental Ag remaining in the samples.

Sintering temperature	AgMg wt. %	Ag wt. %
573 K	91.8	8.2
623 K	95.1	4.9
673 K	96.2	3.8

Table 2: phase fractions of pellets sintered from 12 h ball milled Ag and Mg powder at three different temperatures
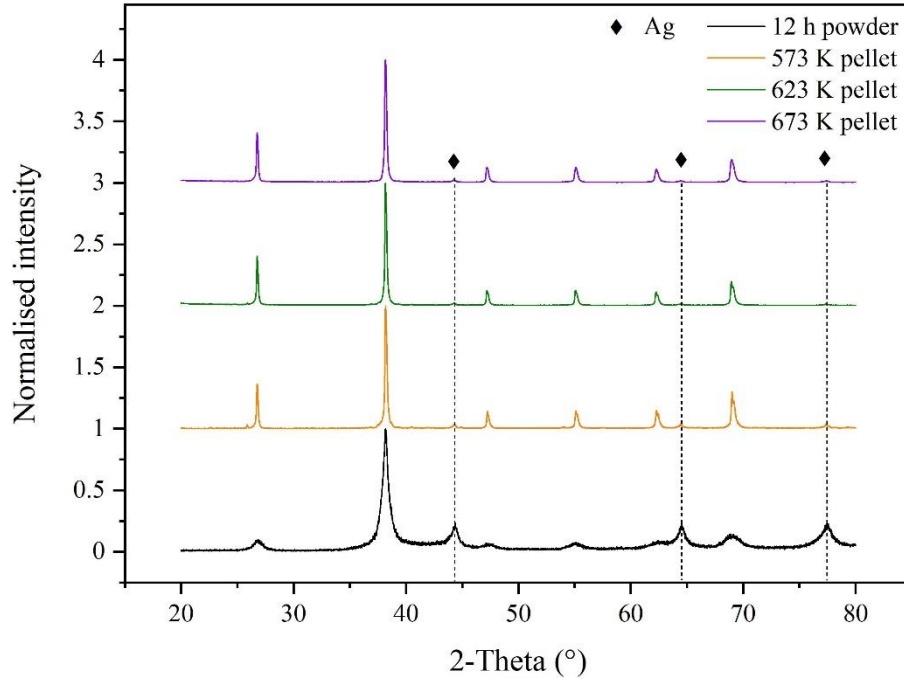

Figure 2: XRD scans for Mg and Ag powder and pellets sintered from this powder at three different temperatures.

3.3. Reduction of initial particle size

In a third approach to consolidate AgMg as completely as possible, the Ag granules are replaced by Ag powder. The synthesis process is identical to the reference, as described in section 2. The replacement of granules (1-6 mm) by powder (<45 μm), is believed to reduce the time necessary to obtain a complete solid state reaction between Ag and Mg through enhancement of effective surface area. After just 8 hours of HEBM, we obtain powder with <1 wt. % Ag.

3.4. Comparison of AgMg precursors and correlation to final composition of MgAgSb

After adding Sb to the precursors obtained through the four different processes described (reference as described in section 2 and three strategies to consolidate AgMg), $MgAg_{0.97}Sb_{0.995}$ samples are sintered, and their composition, microstructure and thermoelectric properties can be compared and related to the precursor formation. The synthesis process after adding Sb is the same in all cases.

For all sintered samples it is possible to correlate the Ag wt. % in the AgMg powder and the final Ag_3Sb wt. %, as stated in Table 3. The phase composition of all four samples is determined from the XRD scans in Figure 3. The amount of dyscrasite decreases with decreasing Ag wt. % in the AgMg precursor. This correlation, however, is not linear: from sample 8-g to 12s-g the reduction of Ag wt. % in the precursor is ~23 %, resulting in a 0.8 % difference in Ag_3Sb wt. % in the final sample; between 12s-g and 30-g a much lower difference in Ag wt. % in the

precursor translates into a larger reduction of final dyscrasite content. It must be pointed out, however, that the phase composition is given in weight %, not in atomic %, which could lead to some misunderstandings. A 1-point difference in Ag wt. % is larger in terms of atomic % than the same change in Ag_3Sb wt. %. In the case of samples 8-g, 30-g and 8-p we also observe Sb as an impurity. The explanation for this remains unclear, but it could be attributed to AgMg powder sticking to the walls of the stainless steel jars, due to its ductility, rendering the mix slightly AgMg-deficient. After the first milling step, Sb is added to the same jar, without emptying or cleaning it. It is possible that some of the powder stuck to the walls of the jar or to the balls does not react with the Sb, thus the appearance of Sb impurities. In the case of sample 12s-g, the jar is cleaned before crushing the sintered pellet to prevent having unreacted powder and use strictly the product of the sintering step.

Sample	Ag wt. % in precursor powder	Ag_3Sb wt. % in final MgAgSb sample	Sb wt. % in final MgAgSb sample	AgMg precursor formation strategy
8-g	26.5	4.9	4.3	8 hours HEBM, Ag granules
30-g	2.5	2.8	4.6	30 hours HEBM, Ag granules
12s-g	3.8	4.1	0	12 hours HEBM followed by sintering at 673 K and crushing, Ag granules
8-p	<1	-	1.3	8 hours HEBM, Ag powder

Table 3: Ag wt. % in AgMg precursor and resulting impurity content in MgAgSb. For the sample names, the number stands for ball-milling times, "g" indicates Ag granules were used, "p" indicates powder was used and "s" indicates a sintering step was included in the obtention of the AgMg precursor
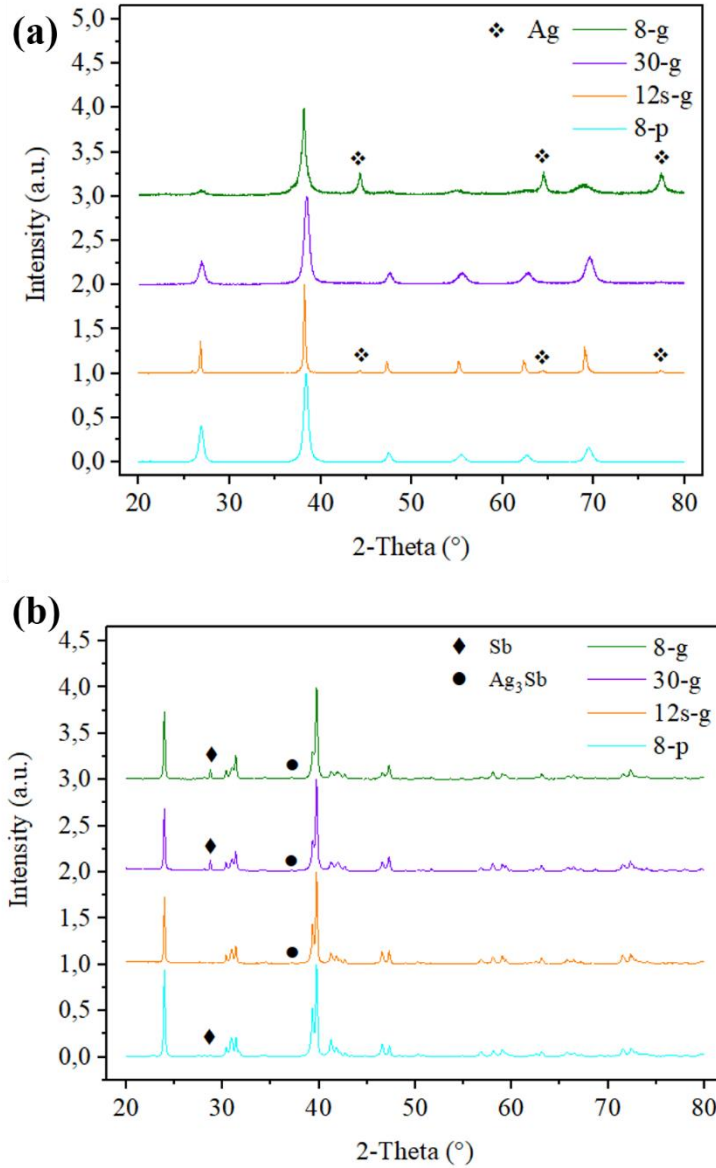
Figure 3: XRD scans for (a) AgMg precursors and (b) compacted MgAgSb pellets obtained with those 4 different AgMg precursors

The microstructure of the different samples is also an indicator of the total impurity content, with 8-p being the most homogenous. Ag_3Sb appears in the form of very defined grains with distinct boundaries, whereas Sb is found as a more diffuse phase, with cloudy boundaries to the MgAgSb matrix (see Figure 4). This might be an indication that it precipitated from the matrix.
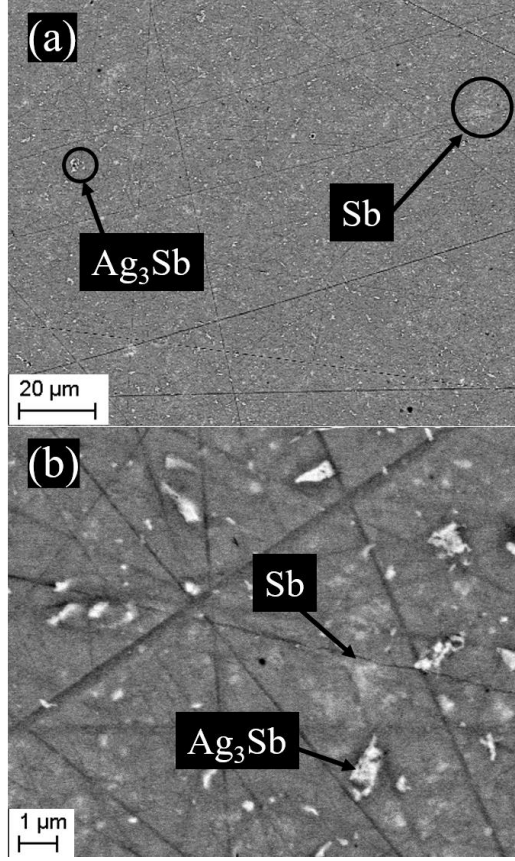
Figure 4: Microstructure of sample 8-g at different magnitudes, showing Sb and Ag₃Sb impurities.

In terms of thermoelectric properties, we can see the best performing sample is 8-p, with a peak zT of ~1.2 at 460 K and an average value of ~1 between RT and 563 K. The Seebeck coefficient curves follow a very similar shape for all samples, with different values, but always showing a maximum close to 350 K (a slightly lower temperature than for the reference curve from Liu et al.[21]). The lower the total impurity content in the sample, the higher the values of S at RT, which are very similar to those found by Liu et al. At higher temperatures, the differences are enlarged, with the samples from this study showing a steeper decrease than the reference data. A similar observation can be made for σ: At 300 K 8-p shows the highest conductivity, and 8-g the lowest. However, the curves of all 4 samples do not follow the same trend: 8-g and 30-g, the samples with the highest impurity content, have their minima at lower temperatures, and the slope after this minimum is steeper than for the other two samples. For thermal conductivity, again, there seems to be a correlation with impurity wt. %, with 12s-g and 8-p having the lowest values, even lower than the reference (0.78 W·m⁻¹·K⁻¹ for 12s-g at 298 K).

Using a single parabolic band (SPB) model we can estimate the charge carrier concentration and mobility at room temperature [17,18]. The reduced chemical potential η is calculated using the experimentally obtained S:

$$S = \frac{k_B}{e}\left(\frac{2F_1(\eta)}{F_0(\eta)} - \eta\right), \tag{1}$$

with k_b being the Boltzmann constant and $F_j(x)$ the Fermi integral of order j. Assuming an effective mass m^* of 2.7·m$_e$ [21], we estimate carrier concentration n:

$$n = 4\pi\left(\frac{2m^*k_BT}{h^2}\right)^{1.5} F_{\frac{1}{2}}(\eta), \tag{2}$$

8

where h is Planck's constant. This value of n is then used together with σ to estimate the corresponding mobility:

$$\mu = \frac{\sigma}{n \cdot e} \tag{3}$$

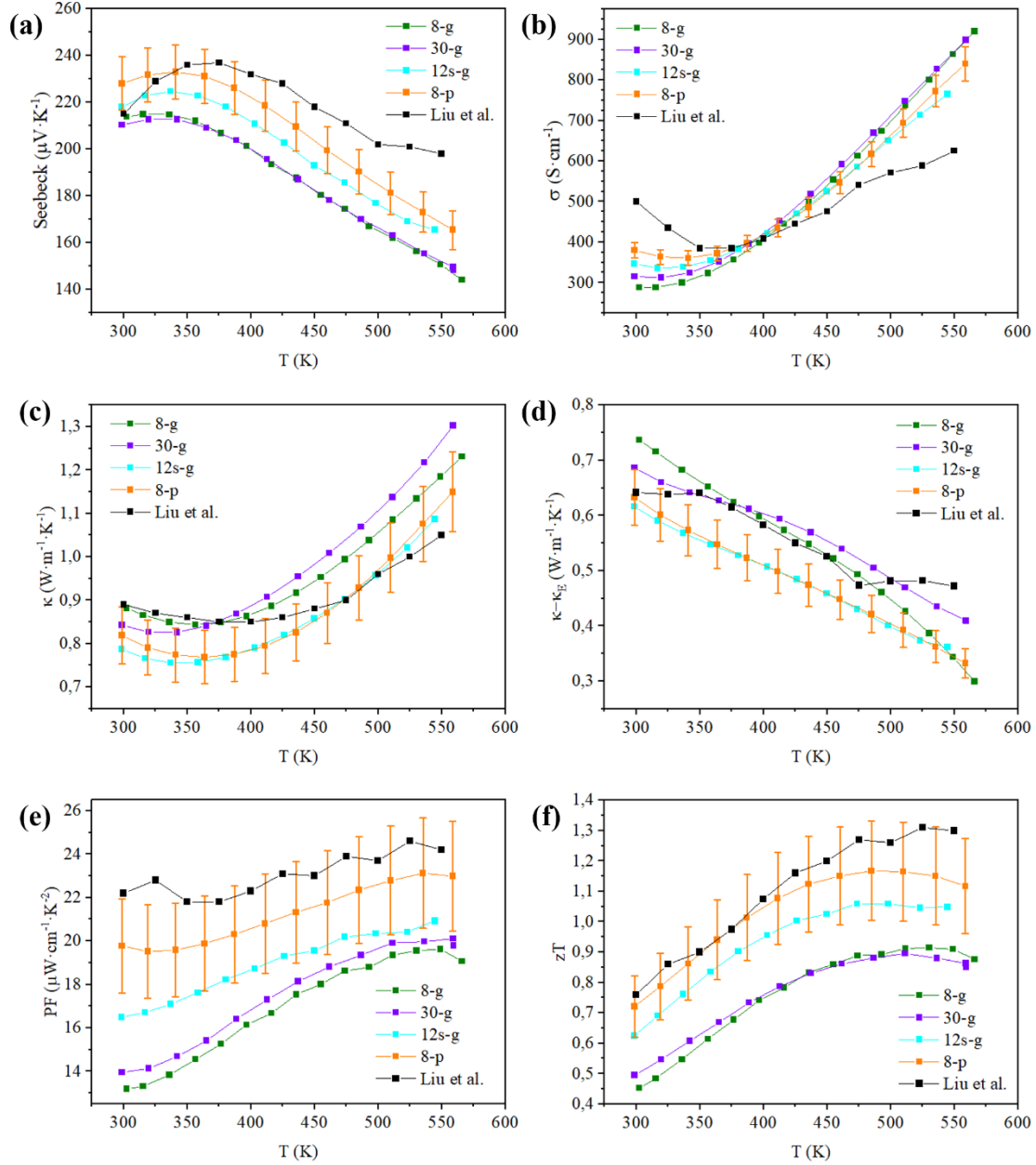The values for n and μ estimated through (2) and (3) are reported in Table 4.

Figure 5: (a) Seebeck coefficient, (b) electrical conductivity, (c) thermal conductivity, (d) lattice and bipolar contributions to the thermal conductivity, (e) power factor and (f) figure of merit for the samples obtained using three different AgMg precursors. Literature values correspond to $MgAg_{0.97}Sb_{0.995}$ as reported by Liu et al. [21]

Sample	n (cm^{-3}) ($\cdot 10^{19}$)	μ (cm$^2 \cdot$V$^{-1} \cdot$s^{-1})
8-g	8.1	22
30-g	8.4	23
12s-g	7.7	28

| **8-p** | 6.7 | 35 |

Table 4: charge carrier concentration and mobility estimations (at room temperature) for all samples. Estimations were obtained assuming a single parabolic band model

From all the different strategies tested, there seems to be a clear correlation between the degree of AgMg formation and the secondary phase content in the final MgAgSb samples, mainly on Ag_3Sb wt. %. These impurities then have an impact on the final thermoelectric properties.

Extending the first ball milling step up to 30 hours is proven to increase reaction between Mg and Ag, improving the AgMg formation compared to the reference route, leading to lower dyscrasite content in MgAgSb sample 30-g. However, the remaining 2.5 Ag wt. % indicates that this is an insufficient solution. In addition, it is considerably time consuming, which could be a problem in terms of process upscalability. Despite the reduction of dyscrasite, we find unimproved overall thermoelectric properties for the long ball milling duration, possibly linked to the increased Sb content.

The combination of milling and sintering forms an AgMg precursor with a relatively high degree of conversion which results in samples (12s-g) with a superior thermoelectric performance compared to 8-g and 30-g. The Ag content is higher in the precursor for 12s-g (3.8 wt% vs 2.5 wt% for 30-g). However, it must be taken into account that for 12s-g the phase quantification has been obtained from sintered material while that of 30-g from powder after ball milling, without a sintering step. Due to the high kinetic impact of ball milling amorphous material can be created that does not show as clear peaks in an XRD scan but can become crystalline after sintering [40–42]. This will lead to an apparently lower secondary phase content in non-sintered material and needs to be taken into account when comparing the phase quantifications. Moreover, the overall secondary phase content is much reduced for the MgAgSb sample from ball milled and sintered AgMg, resulting in an improvement of the thermoelectric properties. However, the additional step in the process can be challenging and introduces complexity to the process.

Replacing the initial Ag granules by powder (reducing the initial particle size) seems to be the overall best solution to prevent the formation of Ag_3Sb and improve the thermoelectric properties of MgAgSb. 8-p presents the lowest secondary phase content and the best zT (average of 0.95 between 300 and 565 K compared to 0.77 for 8-g) of all 4 samples examined, with no lengthening or added complexity to the process as compared to the baseline.

From the results of all different synthesis routes, we can correlate the final content of dyscrasite with that of Ag in the precursor powder, with a good consolidation of AgMg resulting in the desired reduction of Ag_3Sb. The appearance of Sb in the final samples, however, does not seem to be directly affected by the amounts of elemental Ag in the precursor (there is no clear trend in that regard).

As we investigate the thermoelectric properties, we see clear and consistent differences between the different samples, which can be partially explained by their composition and microstructure. Overall, the behavior of all samples follows the same patterns, with the intrinsic regimes starting around 350 K. For p-type thermoelectric materials, this is characterized by a decrease in S and an increase in σ, as observed in Figure 5. From the values of S and σ at room temperature, it is clear that 8-p has a lower carrier concentration n than the other three samples, while having a higher mobility μ, allowing it to have the highest PF of all 4 samples. 8-g and 30-g have very similar behaviors regarding S and σ, both clearly lower at room temperature than 8-p and 12s-g. All these differences are most probably due to the total impurity content: the higher the wt. % of these secondary phases, the higher the carrier concentration and the lower the mobility of these carriers. If we observe the evolution of electrical conductivity at higher temperatures, in the intrinsic regime, we see the tendency is reversed, with 8-g and 30-g having a steeper increase

than the other two samples, resulting in higher values above 400 K. This could possibly be explained by a higher concentration of minority charge carriers and/or a higher mobility of these. From this, and establishing a correlation with Sb wt. %, it is possible to deduce Sb as a major contributor to minority charge carrier concentration. Between 12s-g and 8-p we see a slightly higher slope in σ at high T for the latter, which can be attributed to the higher mobility of charge carriers.

Concerning thermal conductivity, the values at RT for all our samples are lower than the reference, some within the error range. At higher temperatures we once again observe a steeper increase than for the reference, presumably due to the bipolar thermal conductivity. In terms of the lattice contribution, it is lower through the studied temperature range for 8-p and 12s-g (as compared to 8-g, 30-g and the reference values). From the estimated charge carrier mobility values, one might expect 8-g and 30-g to have lower κ_{lat}, due to the phonon scattering by the impurity phases, in line with the observed trend in the carrier mobility. However, in our calculation we are considering the bipolar contribution to thermal conductivity as part of this κ_{lat} (thus the notation κ-κ_E in Figure 5), which is not negligible. The high amounts of Ag_3Sb and Sb might have several, partially compensating effects: whilst on the one hand they presumably scatter phonons reducing the lattice contribution of the thermal conductivity, they will increase the thermal conductivity, as Ag_3Sb and Sb themselves have higher thermal conductivities than MgAgSb and they furthermore influence the carrier concentration which affects the bipolar contribution. We also note a roughly linear decrease of $\kappa - \kappa_e$, but no visible increase at higher temperatures due to the bipolar contribution to the thermal conductivity. This peculiar behavior has been previously observed [15,16,21,26,39,40], and might be due to the limitations of treating the data using a single parabolic band approach [45].

In general, the differences between the expected and the obtained values can be explained through the transport properties n and μ. Both the decrease in carrier concentration and the increase in mobility are presumably a consequence of the reduction in total impurity content and the effect this has on the MgAgSb matrix. Impurities can have both advantageous and detrimental effects in semiconductors, and the compromise between them is undoubtedly complex [9,46,47]. However, in our case they apparently have essentially a negative effect on the properties, as we observe a significant reduction of the mobility and no reduction of the lattice thermal conductivity. The details depend of course on the species of secondary phases, but similar trends have been observed previously for MgAgSb [18,21,30]. Impurities have a scattering effect in both phonons and charge carriers due to the change in grain boundaries and microstructure. The inhomogeneity resulting from these secondary phases could induce significant scattering of both charge carriers and phonons, resulting in lower mobility values. This is consistent with the results found, with mobility decreasing with increasing impurity wt. %. As for the carrier concentration, Ag- and Sb-based impurities could entail an increase in vacancies in the matrix, which would result in higher carrier concentration. Liu et al. suggested that a slight increase in Sb content in the matrix induces Mg and Ag vacancies, since MgAgSb can be expressed as $Mg^{+2}Ag^{+1}Sb^{-3}$ [21]. This probably applies only for impurity-free samples. In our case, the assumption that a lower wt. % of Sb as an impurity implies a larger content of Sb in the matrix, thus inducing vacancy formation cannot be confirmed, since there are other impurities in play (namely dyscrasite), and our matrix cannot be considered to have the nominal composition. In addition to this, both dyscrasite and antimony present semimetallic behaviors, which could affect the carrier concentration regardless of their effect on vacancy creation. Further research should aim at disentangling what the contribution of the impurities themselves is to the trends observed in n and μ and what is due to the changes in the matrix (suspected increase number of vacancies), but it seems clear that both have a major impact in the transport properties and thermoelectric properties of α-MgAgSb.

4. Conclusion

In this work we have shown the correlation between the degree of AgMg formation and the final amount of dyscrasite in MgAgSb. Consolidating AgMg before adding Sb results in a lower content of impurities, which improves the thermoelectric properties of the samples. HEBM is proven to be an effective way to induce solid state reaction between Ag and Mg through mechanical alloying, but it is strongly dependent on initial particle size. Combining ball milling and sintering provides a faster reaction between both elements, but adds complexity to the process, reducing its upscalability. Through changes in the initial step of the process, the average value of zT between 300 and 563 K is improved from 0.77 to 0.95 (~23 %), with a peak value of 1.2 at 500 K when using Ag powder. In general, the synthesis of pure MgAgSb is proven to be challenging, but choosing the individual steps carefully, proper consolidation of AgMg can be achieved, reducing or completely preventing the impurity Ag_3Sb in the final samples and improving the thermoelectric performance.

Author contributions: Ignacio Rodriguez-Barber: Investigation, Validation, Writing - Original Draft; Julia Camut: Investigation, Writing – Review & Editing; Laura Luhmann: Investigation, Writing – Review & Editing; Johannes de Boor: Conceptualization, Supervision, Writing – Review & Editing; Aidan Cowley: Supervision, Writing – Review & Editing; Eckhard Mueller: Supervision, Writing – Review & Editing

References

[1]   D. Champier, "Thermoelectric generators: A review of applications," *Energy Conversion and Management*, vol. 140. Elsevier Ltd, pp. 167–181, 2017.

[2]   S. B. Riffat and X. Ma, "Thermoelectrics: A review of present and potential applications," *Applied Thermal Engineering*, vol. 23, no. 8. pp. 913–935, 2003.

[3]   A. Mazzetti, M. Gianotti Pret, G. Pinarello, L. Celotti, M. Piskacev, and A. Cowley, "Heat to electricity conversion systems for moon exploration scenarios: A review of space and ground technologies," *Acta Astronautica*, vol. 156. IAA, pp. 162–186, 2019.

[4]   J. Yang and T. Caillat, "Thermoelectric Materials for Space Cooling," in *Energy Conversion for Space Power*, vol. 31, no. March 2006, 1961, pp. 111–121.

[5]   M. S. El-Genk, H. H. Saber, and T. Caillat, "Efficient segmented thermoelectric unicouples for space power applications," *Energy Convers. Manag.*, vol. 44, no. 11, pp. 1755–1772, 2003.

[6]   R. C. O'Brien, R. M. Ambrosi, N. P. Bannister, S. D. Howe, and H. V Atkinson, "Safe radioisotope thermoelectric generators and heat sources for space applications," *J. Nucl. Mater.*, vol. 377, no. 3, pp. 506–521, 2008.

[7]   G. S. Nolas, J. Poon, and M. Kanatzidis, "Recent developments in bulk thermoelectric materials," *MRS Bull.*, vol. 31, no. 3, pp. 199–205, 2006.

[8]   S. Chen and Z. Ren, "Recent progress of half-Heusler for moderate temperature thermoelectric applications," *Mater. Today*, vol. 16, no. 10, pp. 387–395, 2013.

[9]   G. J. Snyder and E. S. Toberer, "Complex thermoelectric materials. Nature Materials 7, 105–114.," *Nat. Mater.*, vol. 7, no. February, pp. 105–114, 2008.

[10]   Y. Gelbstein, Z. Dashevsky, and M. P. Dariel, "High performance n-type PbTe-based materials for thermoelectric applications," *Phys. B Condens. Matter*, vol. 363, no. 1–4, pp. 196–205, 2005.

[11]   S. R. Culp, S. J. Poon, N. Hickman, T. M. Tritt, and J. Blumm, "Effect of substitutions on the thermoelectric figure of merit of half-Heusler phases at 800°C," *Appl. Phys. Lett.*, vol. 88, no. 4, pp. 1–3, 2006.

[12]   Z. Liu *et al.*, "Mechanical properties of nanostructured thermoelectric materials α-MgAgSb," *Scr. Mater.*, vol. 127, pp. 72–75, 2017.

[13]   W. Gao *et al.*, "The critical role of boron doping in the thermoelectric and mechanical properties of nanostructured α-MgAgSb," *J. Mater. Chem. C*, vol. 6, no. 36, pp. 9821–9827, 2018.

[14]   M. J. Kirkham, A. M. Dos Santos, C. J. Rawn, E. Lara-Curzio, J. W. Sharp, and A. J. Thompson, "Abinitio determination of crystal structures of the thermoelectric material MgAgSb," *Phys. Rev. B - Condens. Matter Mater. Phys.*, vol. 85, no. 14, pp. 1–7, 2012.

[15]   Y. Zheng *et al.*, "Cost effective synthesis of p-type Zn-doped MgAgSb by planetary ball-milling with enhanced thermoelectric properties," *RSC Adv.*, vol. 8, no. 62, pp. 35353–35359, 2018.

[16]   Y. Zheng *et al.*, "Extraordinary thermoelectric performance in MgAgSb alloy with ultralow thermal conductivity," *Nano Energy*, vol. 59, no. February, pp. 311–320, 2019.

[17]   J. Lei, D. Zhang, W. Guan, Z. Cheng, C. Wang, and Y. Wang, "Engineering electrical transport in α-MgAgSb to realize high performances near room temperature," *Phys. Chem. Chem. Phys.*, vol. 20, no. 24, pp. 16729–16735, 2018.

[18] P. Ying *et al.*, "High performance α-MgAgSb thermoelectric materials for low temperature power generation," *Chem. Mater.*, vol. 27, no. 3, pp. 909–913, 2015.

[19] S. Li *et al.*, "Enhanced thermoelectric properties in MgAgSb composite with Ag3Sb fabricated by the microwave-assisted process and subsequent spark plasma sintering," *Adv. Appl. Ceram.*, vol. 119, no. 2, pp. 107–113, 2020.

[20] H. Zhao *et al.*, "High thermoelectric performance of MgAgSb-based materials," *Nano Energy*, vol. 7, pp. 97–103, 2014.

[21] Z. Liu *et al.*, "Effects of antimony content in MgAg0.97Sbx on output power and energy conversion efficiency," *Acta Mater.*, vol. 102, pp. 17–23, 2016.

[22] Z. Liu *et al.*, "Lithium Doping to Enhance Thermoelectric Performance of MgAgSb with Weak Electron-Phonon Coupling," *Adv. Energy Mater.*, vol. 6, no. 7, pp. 1–11, 2016.

[23] J. Shuai *et al.*, "Study on thermoelectric performance by Na doping in nanostructured Mg1-xNaxAg0.97Sb0.99," *Nano Energy*, vol. 11, pp. 640–646, 2015.

[24] Z. Liu *et al.*, "The influence of doping sites on achieving higher thermoelectric performance for nanostructured α-MgAgSb," *Nano Energy*, vol. 31, no. October 2016, pp. 194–200, 2017.

[25] J. Sui *et al.*, "Effect of Cu concentration on thermoelectric properties of nanostructured p-type MgAg0.97-xCuxSb0.99," *Acta Mater.*, vol. 87, pp. 266–272, 2015.

[26] X. Li *et al.*, "Ultralow thermal conductivity from transverse acoustic phonon suppression in distorted crystalline α-MgAgSb," *Nat. Commun.*, vol. 11, no. 1, 2020.

[27] T. W. Lan *et al.*, "Enhancing the figure of merit in thermoelectric materials by adding silicate aerogel," *Mater. Today Phys.*, vol. 13, pp. 0–6, 2020.

[28] D. Li *et al.*, "Atomic Disorders Induced by Silver and Magnesium Ion Migrations Favor High Thermoelectric Performance in α-MgAgSb-Based Materials," *Adv. Funct. Mater.*, vol. 25, no. 41, pp. 6478–6488, 2015.

[29] A. B. R. T. Frost and G. V Raynor, "The system silver-magnesium-antimony, with reference to the theory of alloy formation," *Proc. R. Soc. London. Ser. A. Math. Phys. Sci.*, vol. 203, no. 1072, pp. 132–147, 1950.

[30] J. Camut *et al.*, "Insight on the interplay between synthesis conditions and thermoelectric properties of α-MgAgSb," *Materials (Basel).*, vol. 12, no. 11, 2019.

[31] H. Kamila *et al.*, "Analyzing transport properties of p-type Mg 2 Si-Mg 2 Sn solid solutions: Optimization of thermoelectric performance and insight into the electronic band structure," *J. Mater. Chem. A*, vol. 7, no. 3, pp. 1045–1054, 2019.

[32] A. Sankhla *et al.*, "Mechanical Alloying of Optimized Mg 2 (Si,Sn) Solid Solutions: Understanding Phase Evolution and Tuning Synthesis Parameters for Thermoelectric Applications," *ACS Appl. Energy Mater.*, vol. 1, no. 2, pp. 531–542, 2018.

[33] M. Yasseri *et al.*, "Solid solution formation in Mg2(Si,Sn) and shape of the miscibility gap," *Acta Mater.*, vol. 185, pp. 80–88, 2020.

[34] L. Song, J. Zhang, and B. B. Iversen, "Thermal stability of p-type Ag-doped Mg3Sb2 thermoelectric materials investigated by powder X-ray diffraction," *Phys. Chem. Chem. Phys.*, vol. 21, no. 8, pp. 4295–4305, 2019.

[35] J. Zhang, L. Song, A. Mamakhel, M. R. V. Jørgensen, and B. B. Iversen, "High-Performance Low-Cost n-Type Se-Doped Mg3Sb2-Based Zintl Compounds for Thermoelectric Application," *Chem. Mater.*, vol. 29, no. 12, pp. 5371–5383, 2017.

[36] Q. Zhu, S. Song, H. Zhu, and Z. Ren, "Realizing high conversion efficiency of Mg3Sb2-based thermoelectric materials," *J. Power Sources*, vol. 414, no. January, pp. 393–400, 2019.

[37] J. De Boor *et al.*, "High-temperature measurement of seebeck coefficient and electrical conductivity," *J. Electron. Mater.*, vol. 42, no. 7, pp. 1711–1718, 2013.

[38] A. A. Nayeb-Hashemi and J. B. Clark, "The Ag-Mg (Silver-Magnesium) system," *Bull. Alloy Phase Diagrams*, vol. 5, no. 4, p. 348, 1984.

[39] A. F. May and G. J. Snyder, "Introduction to modeling thermoelectric transport at high temperatures," *Mater. Prep. Charact. Thermoelectr.*, pp. 11-1-11–18, 2017.

[40] V. Ramachandran and J. Beaudoin, *Handbook of analytical techniques in concrete science and technology: principles, techniques and applications*. Elsevier, 2000.

[41] H. Minor and C. Technology, "General procedure for evaluating amorphous scattering and crystallinity from X-ray diffraction scans of semicrystalline polymers," *Polymer (Guildf).*, vol. 31, pp. 996–1002, 1989.

[42] C. Nunes, A. Mahendrasingam, and R. Suryanarayanan, "Quantification of crystallinity in substantially amorphous materials by synchrotron X-ray powder diffractometry," *Pharm. Res.*, vol. 22, no. 11, pp. 1942–1953, 2005.

[43] G. Zhou, J. wen Xu, and G. hui Rao, "Hole doped α-MgAgSb as potential low temperature thermoelectric materials," *Phys. Lett. Sect. A Gen. At. Solid State Phys.*, vol. 383, no. 26, p. 125833, 2019.

[44] N. Miao and P. Ghosez, "Optimization of thermoelectric properties of MgAgSb-based materials: A first-principles investigation," *J. Phys. Chem. C*, vol. 119, no. 25, pp. 14017–14022, 2015.

[45] S. Wang, J. Yang, T. Toll, J. Yang, W. Zhang, and X. Tang, "Conductivity-limiting bipolar thermal conductivity in semiconductors," *Sci. Rep.*, vol. 5, pp. 1–9, 2015.

[46] T. Zhu, Y. Liu, C. Fu, J. P. Heremans, J. G. Snyder, and X. Zhao, "Compromise and Synergy in High-Efficiency Thermoelectric Materials," *Adv. Mater.*, vol. 29, no. 14, 2017.

[47] E. S. Toberer, A. Zevalkink, and G. J. Snyder, "Phonon engineering through crystal chemistry," *J. Mater. Chem.*, vol. 21, no. 40, pp. 15843–15852, 2011.